Biophysical Journal
Article

Biophysical Society

K-Ras4B Remains Monomeric on Membranes over a Wide Range of Surface Densities and Lipid Compositions

Jean K. Chung,[1] Young Kwang Lee,[1] John-Paul Denson,[3] William K. Gillette,[3] Steven Alvarez,[2] Andrew G. Stephen,[3] and Jay T. Groves[1,*]

[1]Department of Chemistry and [2]Department of Materials Science and Engineering, University of California Berkeley, Berkeley, California; and [3]NCI RAS Initiative, Cancer Research Technology Program, Frederick National Laboratory for Cancer Research, Leidos Biomedical Research, Inc., Frederick, Maryland

ABSTRACT Ras is a membrane-anchored signaling protein that serves as a hub for many signaling pathways and also plays a prominent role in cancer. The intrinsic behavior of Ras on the membrane has captivated the biophysics community in recent years, especially the possibility that it may form dimers. In this article, we describe results from a comprehensive series of experiments using fluorescence correlation spectroscopy and single-molecule tracking to probe the possible dimerization of natively expressed and fully processed K-Ras4B in supported lipid bilayer membranes. Key to these studies is the fact that K-Ras4B has its native membrane anchor, including both the farnesylation and methylation of the terminal cysteine, enabling detailed exploration of possible effects of cholesterol and lipid composition on K-Ras4B membrane organization. The results from all conditions studied indicate that full-length K-Ras4B lacks intrinsic dimerization capability. This suggests that any lateral organization of Ras in living cell membranes likely stems from interactions with other factors.

INTRODUCTION

Ras is a protein of paramount clinical importance with its oncogenic mutations correlated with 30% of all human cancers (1). Its principal function as a membrane-anchored GTPase is to serve as a molecular switch; when bound to GDP, Ras remains inert, but when GDP is exchanged to GTP, a conformational change allows interaction with downstream effectors and signal propagation. On the cell membrane surface, some reports have suggested Ras is ordered into clusters that may be central to signal propagation (2,3). Additionally, direct molecular dimerization of Ras on the membrane has emerged in recent years as a possible underlying mechanism for the lateral organization (4,5). The putative Ras dimer has also attracted attention as an alternative inhibition target for cancers involving hyperactivation of Ras, which to date has proven exceptionally difficult to control with conventional therapeutic drugs (6,7). Although crystal structures of Ras indicate a possible dimer interface, dimers are not generally observed in solution, even at high Ras concentration (8,9). The structure of Ras, however, may be different on the membrane (10,11) and the possibility of a membrane-assisted dimerization or clustering mechanism has attracted much attention (9,12–15). Such mechanisms include membrane-mediated exposure of a dimerization interface and lipid-mediated interactions through the Ras membrane anchor.

Although studies of Ras in cell membranes have revealed nonuniform distributions (2,13,16–18), it is extremely difficult to conclusively determine if this organization is an intrinsic property of Ras or is the result of other interactions within the cellular environment (19,20). A number of studies of purified Ras in lipid vesicles and supported bilayers have yielded mixed conclusions. Studies using fluorescent spectroscopic methods with N- and H-Ras with semisynthetic anchors in supported lipid bilayers reported dimerization (10,11), but a subsequent study found Ras to be exceptionally susceptible to photosensitized oxidative cross linking, which could have affected the fluorescence experiments (21). K-Ras dimers were detected in solution by dynamic light scattering when bound to GTPγS, a sulfuric GTP analog (22). On the other hand, the globular domain of H-Ras was found to be incapable of dimerization when investigated with rotational anisotropy and NMR (23).

Submitted August 18, 2017, and accepted for publication October 30, 2017.

*Correspondence: jtgroves@lbl.gov

Jean K. Chung and Young Kwang Lee contributed equally to this work.

Editor: Arne Gericke.

https://doi.org/10.1016/j.bpj.2017.10.042

Lacking in these studies, however, were the posttranslational modifications of Ras, which are known to be critical for proper membrane localization in cells and could introduce additional interactions within the membrane. Furthermore, possible effects of various lipid headgroups, chain chemistry, and the presence of cholesterol—a major component in the plasma membrane—were largely unexplored in these earlier in vitro studies.

To gain a clearer understanding of Ras dimerization on membranes, and to address potential roles of membrane lipids and cholesterol interacting with the Ras membrane anchor, we reconstituted natively purified K-Ras4B, wild-type, and tagged with eGFP, on supported lipid bilayers (Fig. 1). K-Ras4B is a Ras isoform associated with the highest incidence of oncogenic mutations (24). The purification and characterization of these constructs with complete post-translational modifications has recently been accomplished, thus providing an opportunity for a more thorough investigation of K-Ras4B organization on membranes (25). K-Ras4B is composed of a globular G-domain, a positively charged hypervariable region, and posttranslational modifications including farnesylation and methylation of the terminal cysteine, which provide anchorage to the membrane (26). When introduced to supported lipid bilayers, K-Ras4B spontaneously inserts into the membrane and establishes equilibrium between membrane and solution (Fig. S1). Using this experimental platform, we systematically investigated how key parameters such as protein density on the membrane surface, nucleotide state, and lipid membrane composition (including cholesterol) modulate the behavior of K-Ras4B with quantitative spectroscopic measurements.

Overall, the studies of fully processed K-Ras4B described here reveal universally monomeric behavior across a wide range of surface densities and membrane compositions. Even in cholesterol-containing membranes near a miscibility phase transition, strictly monomeric mobility is observed. Due to both the importance of Ras and its complexity on membranes, we have sought to acquire as comprehensive and quantitatively rigorous data as presently possible to address the question of its dimerization on membranes. These observations indicate that any dimerization or clustering of Ras that may exist in the cell membrane involves additional factors not present in these reconstituted experiments.

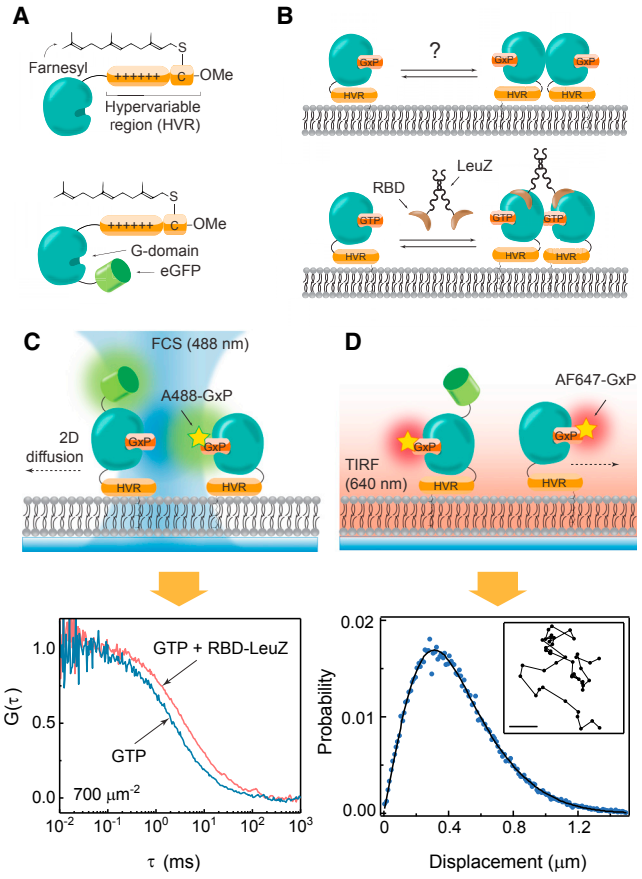

FIGURE 1 Experimental design for K-Ras on SLBs. (*A*) Given here are processed K-Ras4B constructs used in these experiments: wild-type (*top*) and eGFP-labeled (*bottom*). (*B*) Cross-linked dimers formed by RBD fused to LeuZ were used as benchmarks for dimerization for the diffusion measurements. (*C*) Given here is the supported lipid bilayer-based experimental setup for FCS (*top*), and resulting autocorrelation traces for monomeric and cross-linked Ras (*bottom*). (*D*) Shown here is the TIRF microscopy setup for SMT (*top*), and step-size distribution (*bottom*). (*Inset*) This shows an example of SMT trajectories from which the step-size distributions are obtained; scale bar: 10 μm. To see this figure in color, go online.

MATERIALS AND METHODS

Protein preparation

K-Ras4B and eGFP-K-Ras4B. The complete protocol for purification of fully processed K-Ras4B has been published previously (25). For eGFP-K-Ras4B, the linker was GSG. The full amino acid sequence can be found in the Supporting Material. FNTA and FNTB, the human enzymes responsible for the first posttranslational modification (farnesylation), are introduced into the baculovirus/insect expression system by cloning the respective genes into the same baculovirus genome as the K-Ras4B expression construct. Insect proteins presumably carry out the subsequent post-translational modification steps of C-terminal proteolysis (removing the C-terminal amino acid tripeptide of Val-Ile-Met and the hydroxymethylation of the C-terminal carboxyl group). K-Ras4B is expressed as the fusion protein His6-MBP-tev-K-Ras4B (His6, six-histidine affinity tag; MBP, maltose binding protein to enhance solubility; tev, TEV protease recognition site). Briefly, the expressed protein is captured from Tni-FNL cells (a cell line of *Trichoplusia ni* isolated at the Frederick National Laboratory) after lysis of the pellet (harvested 72 h postinfection from cultures incubated at 21°C) by immobilized metal-ion chromatography (IMAC). The fusion protein is buffer-exchanged to a lower salt and lower pH buffer (MES pH 6.0), bound to an SP sepharose column, and eluted with a moderate salt buffer. The fusion protein is then cleaved by the addition of a His6-TEV protease and simultaneously buffer-exchanged back to a neutral pH buffer. The final chromatographic step is to remove the His6-tagged contaminants from the TEV protease reaction (His6-TEV protease, non-cleaved fusion protein, and His6-MBP) using another IMAC step (the non-His-tagged target protein has a low affinity for the IMAC resin but is well resolved from the contaminants in the column elution). The protein is dialyzed to remove the trace amounts of imidazole from the column elution, concentrated as necessary. The molecular weight of the processed

K-Ras4B and eGFP-K-Ras4B was confirmed by SDS-PAGE and intact electrospray ionization mass spectrometry, shown in Fig. S1. The mass spectra for both K-Ras4B and eGFP-K-Ras4B show negligible abundance for unlipidated (−380 Da) species.

The Ras binding domain fused to leucine zipper (RBD-LeuZ) and the catalytic domain of Son of Sevenless (SOScat). Ras binding domain (RBD) (residues 56–131) of cRaf (accession number: BC018119) with N-terminal SNAP tag and Leucine zipper (LeuZ, amino acid sequence: YKQLEDKVEELASKNYHLENEVARLKKLVEF) was cloned into a modified pETM-33 vector (European Molecular Biology Laboratory, Heidelberg, Germany) using the *Kpn*I/*Not*I sites. The expression vector fuses an N-terminal His_6-GST-PreScission cleavage sequence (pr)-SNAP tag (SNAP) to RBD, creating His6-GST-pr-SNAP-LeuZ-RBD. SOS_{cat} Cys-lite (residues 566–1049 with the following mutations: C838A, C635A, C980S, and E718C) of human SOS1 (accession number: AK290228.1) was cloned in the expression vector pProEx HTb (Invitrogen, Carlsbad, CA) using *Nco*I/*Hin*dIII sites. The vector fuses an N-terminal His_6 Tag-Tev sequence to SOS_{cat}. The detailed protein purification protocol for SOS_{cat} has been published previously (27). A similar protocol was also used for purification of RBD-LeuZ. RBD-LeuZ and SOS_{cat} were expressed in *Escherichia coli* (BL21 DE3) cells and purified using an N-terminal His_6 tag. After elution from a HiTrap Chelating HP column (GE Healthcare, Little Chalfont, UK), the His_6-GST tag for RBD-LeuZ and His_6 tag for SOS_{cat} was cleaved by incubation of the protein with the TEV and PreScission protease, respectively. The cleavage reaction was carried out overnight at 4°C, while dialyzing in 50 mM PBS (pH 8.0), 300 mM NaCl and 0.4 mM 2-mercaptoethanol. The proteins were further purified by size-exclusion chromatography on a Superdex 75 column (GE Healthcare) that was equilibrated in gel-filtration buffer (20 mM Tris-HCl pH 8.0, 200 mM NaCl, 10% glycerol (v/v), and 1 mM tris(2-carboxyethyl)phosphine (Cat. No. C4706; Sigma-Aldrich, St. Louis, MO).

Supported lipid bilayer formation

Planar-supported lipid bilayers (SLBs) of varying compositions consisting primarily of 1,2-dioleoyl-*sn*-glycero-3-phosphocoline (DOPC, Cat. No. 850375C; Avanti Polar Lipids, Alabaster, AL) were prepared for fluorescence microscopy. The detailed protocol has been published previously (28). Briefly, SLBs were formed by fusion of small unilamellar vesicles, prepared by probe sonication, on glass substrates cleaned by Piranha etch (5 min in 3:1 H_2SO_4:H_2O_2). Other bilayer components such as phosphatidylinositol (4,5)-bisphosphate (PIP_2), 18:1-18:1 PS (DOPS), and 18:1-18:0 PS (SOPS) were also purchased from Avanti Polar Lipids (Cat. No. 850156P, 840046, and 840035C, respectively). For the visualization of the bilayers, a trace amount (0.005 mol %) of fluorescently labeled lipid, Texas Red DHPE (Cat. No. T1395MP; Thermo Fisher Scientific, Waltham, MA) was included. The bilayers were prepared in sticky-slide VI 0.4 microfluidic chambers (Cat. No. 80608; Ibidi, Munich, Germany) assembled with the glass slide substrate for imaging. The final buffer (pH 7.4) was composed of the following: 40 mM HEPES, 100 mM NaCl, 10 mM BME, and 0.1 mg/mL casein (all purchased from Sigma-Aldrich). BME is critical in preventing photosensitized cross linking that was found to affect Ras during fluorescence experiments (21). The integrity and fluidity of the bilayers and membrane-bound proteins was confirmed by fluorescence recovery after photobleaching or fluorescence correlation spectroscopy (FCS). All experiments were performed at room temperature, 23°C.

Supported lipid bilayer from ruptured giant unilamellar vesicles

Giant unilamellar vesicles (GUVs) were produced by electroformation, closely following a published protocol (29). The lipid compositions (either 10% DOPS vesicles: 0.39/0.1/0.2/0.3/0.01 DOPC/DOPS/DPPC/cholesterol/TR-DHPE, or 20% SOPS vesicles: 0.29/0.2/0.2/0.3/0.01 DOPC/SOPS/DPPC/cholesterol/TR-DHPE) were chosen such that the demixing transition temperature is below the room temperature (30). A quantity of 20 mmol of lipid mixtures in chloroform was deposited in the ITO-coated glass slides (30–40 Ω; Delta Technologies, Dallas, TX), and assembled into a capacitor using a rubber spacer and conductive copper tapes. GUV budding from lipid film was then induced by passing ±2.8 V sine waves at 10 Hz, provided by a waveform generator (Tektronics, Beaverton, OR), through the capacitor for 3 h in 250 mM sucrose solution (osmolarity 270 mOs) at 50°C to maximize homogeneous distribution of lipids. The resulting vesicles were then allowed to adhere and rupture onto Piranha-etched glass coverslip surfaces in HEPES buffer, and were imaged by Texas Red fluorescence.

Ras nucleotide exchange

Native nucleotides bound to K-Ras were exchanged by guanine nucleotide exchange factor SOS (31,32). A quantity of 1 μM of K-Ras was incubated with 0.5 μM of catalytic domain of SOS, SOS_{cat}, in an excess amount of desired nucleotides (1 mM for nonfluorescent nucleotides, and 10 μM for fluorescent nucleotides). Nucleotide exchange reactions were carried out at least 3 h at room temperature.

FCS

The experimental setup for FCS has been described previously (21). Dual-color FCS measurements were performed on a home-built confocal system integrated into a TE2000 inverted microscope with a 100× oil immersion objective (PlanFluor, NA 1.30; Nikon, Melville, NY). The light source was a pulsed (100 ps pulse duration at 19.5 MHz repetition rate) supercontinuum laser (SuperK Extreme; NKT Photonics, Portland, OR), with the wavelengths selected by a combination of dichroic mirrors and bandpass filters, which were directed to the microscope via an optical fiber (Thorlabs, Newton, NJ) in the epifluorescence geometry. The average excitation power for a typical FCS measurement was 0.5 μW for blue light (488 ± 5 nm) and 1.0 μW for orange light (561 ± 5 nm) immediately before the objective. The fluorescent signals were collected by the objective and passed a 50-μm pinhole (Thorlabs) before they were split by a dichroic mirror (Thorlabs). Each signal was focused into 0.15 × 0.15 μm avalanche photodiode elements (Hamamatsu, Hamamatsu City, Japan), and subsequently processed by a hardware correlator (Correlator.com). The resulting autocorrelation $G(\tau)$ traces were fit to 2D Gaussian diffusion model (33),

$$G(\tau) = \frac{1}{N}\left(\frac{1}{1+\tau/\tau_d}\right), \quad (1)$$

where τ is the time delay, N is the number of particles in the focus, and τ_d is the correlation time. To calibrate the spot size of the confocal focus, N of a bilayer with a known surface density of fluorescent lipids of each color, BODIPY-FL-DHPE (Thermo Fisher Scientific) for the blue light and Texas Red-DHPE for the orange light were measured, which consistently yielded the radii of 0.20 ± 0.01 and 0.22 ± 0.01 μm for the blue and orange light, respectively. The diffusion coefficient D was calculated by using the relation

$$D = w^2/4\tau_d, \quad (2)$$

where w is the radius of the focus spot size.

Single-molecule total internal reflectance fluorescence microscopy

The experimental methods for single-molecule total internal reflectance fluorescence (TIRF) has been described previously (21,32). TIRF images

were acquired using an Eclipse Ti inverted microscope (Nikon) equipped with a 100× 1.49 NA oil immersion TIRF objective and an iXon EMCCD camera (Andor Technology, South Windsor, CT). Illumination sources for TIRF imaging in the form of 488- and 637-nm lasers (Coherent, Santa Clara, CA) were used, with ET500LP and ET525/50M filters (Chroma Technology, Bellows Falls, VT) for the 488-nm channel imaging, and ET660LP and ET700/75M filters for 637-nm channel imaging. To track K-Ras at the single-molecule level in a wide range of surface density, 100 pM of Alexa 647-GppNHp-loaded K-Ras was mixed with various concentrations of eGFP-K-Ras loaded with nonfluorescent GppNHp (typically up to 50 nM). TIRF intensity of the eGFP channel was used to estimate the overall density of K-Ras, and Alexa 647-GppNHp-loaded K-Ras was imaged for single-molecule tracking (SMT). Diffusion trajectories were analyzed with the softwares TrackMate (ImageJ plugins; National Institutes of Health, Bethesda, MD) and Igor Pro (WaveMetrics, Lake Oswego, OR). The step size distribution calculated from several thousands of trajectories was fit with the Brownian diffusion model as described by the following equation:

$$p(r,t,D) = \frac{\alpha r}{2D_1 t}\exp\left(-\frac{r^2}{4D_1 t}\right) + \frac{(1-\alpha)r}{2D_2 t}\exp\left(-\frac{r^2}{4D_2 t}\right), \quad (3)$$

where D_1 and D_2 are different diffusion coefficients for fast and slow species, respectively; and α is a relative population for the fast species. For the single-species diffusion model, α is 1, thus eliminating the second term. Fitting residues for the single- and two-component model were monitored to determine the number of diffusion species. The diffusion coefficients and relative population of each component were calculated from the corresponding fitting (see the Supporting Material for more details).

RESULTS AND DISCUSSION

We monitored the K-Ras4B (henceforth referred to simply as "Ras") mobility on the membrane surface to detect dimerization. For all the lipid compositions studied here, membrane-anchored Ras exhibits unencumbered Brownian motion, as described by the Einstein relation,

$$\langle r(t)^2 \rangle = 4Dt = 4\frac{k_B T}{\lambda}t, \quad (4)$$

where r is displacement, t is time, D is the diffusion coefficient, k_B is the Boltzmann constant, T is the temperature, and λ is the drag coefficient. The diffusion coefficient of molecules or particles through a fluid is generally a function of size. In three dimensions, the familiar Stokes-Einstein relation ($D = k_B T/6\pi\eta r$, where η is the fluid viscosity) is widely used as a basis for molecular and particle size determination. The situation in two dimensions, however, is more complex because no such simple scaling between mobility and size exists—a phenomenon known as the Stokes paradox (34,35). Nonetheless, dimerization on membranes is robustly detectable by measuring changes in D resulting from the differing values for λ experienced by monomers and dimers. An additive effect in the frictional drags of dimers has been observed experimentally when well-defined and separated lipid anchors dictate protein diffusion (36–38). However, the actual values of λ generally depend on a complex convolution of many factors such as protein structure, degree of its interaction with the membrane, and the surrounding environment. Furthermore, although quantities such as protein radius have well-defined consequences on diffusion as described by Saffman and Delbrück (34), they are difficult to determine for Ras dimerization. For instance, it cannot be determined, based on currently available information, how much dimerization would increase the effective radius of the protein, given its irregular shape and ambiguous nature of the interaction with the membrane. Therefore, rather than attempting to calculate the theoretical diffusion coefficient of Ras dimers, we experimentally calibrate the differential mobility between a Ras monomer and dimer using a Ras binding domain of c-Raf fused with a leucine zipper (RBD-LeuZ) to induce dimerization in a controlled manner. RBD selectively binds to GTP-bound Ras and LeuZ is a constitutive dimer, therefore its presence creates a population of cross-linked Ras, providing a benchmark for dimerization (Fig. 1 *B*).

For quantitative measurement of Ras diffusion on SLBs, we employed FCS (Fig. 1 *C*) and SMT (Fig. 1 *D*) by TIRF microscopy. Although either method alone is, in principle, sufficient to obtain all of the conclusions derived here, they provide complementary information and we use both to obtain a more complete characterization of Ras mobility on the membrane. Additionally, two different labeling strategies were used to track Ras: eGFP fused at the N-terminus, or nucleotides labeled with extrinsic organic fluorophores, such as ATTO 488 (A488) or AlexaFluor 647 (AF647). The identity of the fluorescent label did not result in any detectable differences in the diffusion behavior of Ras, indicating that the eGFP label does not introduce a significant perturbation.

In FCS, the time-dependent fluorescence fluctuation due to molecules entering and exiting the confocal focus is recorded (Fig. 1 *C*). The autocorrelation function, $G(\tau)$, of these fluctuations of a mixed population in a 2D Gaussian focal spot is given by

$$G(\tau) = \frac{\sum N_i B_i^2 (1+\tau/\tau_i)^{-1}}{\left(\sum N_i B_i\right)^2}, \quad (5)$$

where N_i, B_i, and τ_i are the number of particles, the molecular brightness, and the focus residence time for the ith species, respectively (33). The apparent surface density and diffusion can then be calculated for a calibrated spot size (Eq. 2). Equation 5 indicates that multiple diffusing species may in principle be resolved. In practice, however, the autocorrelation function of a mixed population of two species with diffusion coefficient within an order of magnitude, as is the case for Ras monomers and dimers, cannot be reliably resolved due to the relatively featureless and gently sloping

lineshape of the autocorrelation function (see the Supporting Material). Thus, only the weighted average using single-species model, Eq. 1, is obtained in these experiments. Calibration experiments using the LeuZ dimer reveal that the mobility of monomer and dimer in this experimental system differ by a factor of 2.0 (see the Supporting Material). FCS is particularly advantageous for detection of dimers, even for those with extremely weak affinities, because the presence of a small fraction of brighter dimer contributes nonlinearly to the composite FCS data (see the Supporting Material). This is evident in Eq. 5, where $G(\tau)$ scales with the square of B_i. Therefore, even though the individual contributions from monomers and dimers to the FCS measurements cannot be separated, the measured average is extremely sensitive to a minute fraction of dimers. An additional advantage afforded by FCS is that the surface protein density is directly measured simultaneously with diffusion. As a large range of surface density needed to be examined due to the unknown dimerization affinity, this was particularly expedient.

In SMT, on the other hand, the trajectories of membrane-bound fluorescent molecules at single-molecule level are directly imaged (Fig. 1 *D*, *top*). The diffusion coefficients can be extracted by fitting the measured step-size distribution to the 2D Brownian diffusion model (Fig. 1 *D*, *bottom*). As a single-molecule technique, SMT can resolve two diffusing species with closer diffusion rates compared to FCS, provided that the camera has sufficient time resolution (20 ms in these studies). Additionally, SMT offers the possibility of detecting the timescale of transitions (e.g., between monomer and dimer) as well as the spectrum of different species present on the membrane. In combination, FCS and SMT provide a means of internal self-consistency checking (11).

Dimerization of Ras on the membrane surface is an essentially 2D reaction in which the fraction of dimers at equilibrium is a function of the overall Ras surface density. The 2D dissociation constant, $K_d = [Ras]^2_{2D}/[Ras{\bullet}Ras]_{2D}$, is defined in terms of the equilibrium surface densities of Ras monomer, $[Ras]_{2D}$, and Ras dimer, $[Ras{\bullet}Ras]_{2D}$. It is important to note that this 2D dissociation constant generally cannot be calculated from the corresponding 3D affinity. In the case of Ras as studied here, there are four factors that contribute to the actual 2D K_d: 1) translational entropy, referring to the reduction in spatial dimension from three to two, which is also sometimes called a concentration effect (this one can be easily calculated and generally favors dimerization); 2) rotational entropy, referring to the change in rotational degrees of freedom resulting from membrane anchorage (this may be estimated using protein atomic structure data (11,39), but is complex and can be either positive or negative); 3) structural change, such as those that may result from sitting on the membrane surface (40–42); and 4) lipid anchor-mediated interactions (42,43), in which attractive interactions are mediated through the solvation of the Ras membrane anchor by the surrounding membrane lipids.

As a general strategy in these experiments, we sought to map the 2D Ras-Ras binding curve as a function of Ras density to determine the 2D K_d. Example binding curves for a 2D binding reaction for a variety of 2D K_d values are plotted in Fig. 2 *A*. To provide a rough calibration relating to 3D affinities, if we consider only the translational entropy (concentration) effect, K_d values of 200 and 1.25×10^5 μm^{-2} are equivalent to 3D dissociation constants of 0.1 and 70 mM, respectively (see the Supporting Material for details). Note that a Ras surface density of 1.25×10^5 μm^{-2} corresponds to essentially dense packed on the membrane surface (44), so 2D K_d values in this range correspond to effectively no binding affinity. The density range accessible by FCS is determined by the autocorrelation signal-to-noise ratio, and spans from ~10 to 1500 molecules/μm^2 in this system (corresponding to 2–190 particles per near diffraction-limited focal radius of 200 nm).

FCS measurements reveal a weighted average of the mobility in a system containing a mixture of monomers and dimers. Calculations of the weighted averaged values of *D*, as would be reported by FCS (following Eq. 5 and based on the LeuZ dimer calibration experiment, detailed in the Supporting Material) corresponding to the 2D dimer binding curves in Fig. 2 *A* are plotted in Fig. 2 *B*. For this calculation, experimentally estimated values for the

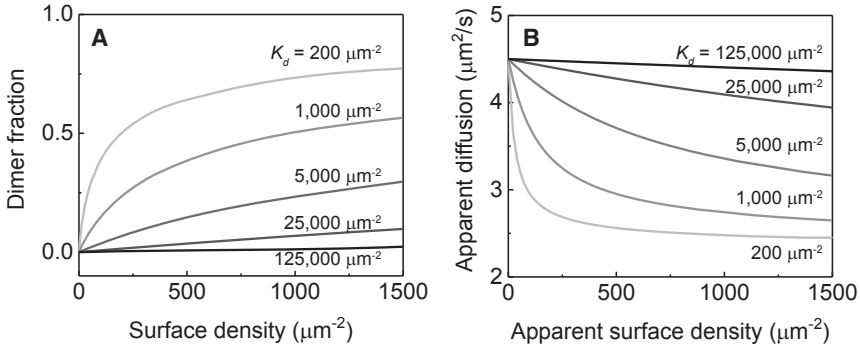

FIGURE 2 Theoretical dynamic range for FCS in dimerization detection. (*A*) Fraction of dimers as a function of surface density for a series of 2D dissociation constants K_d are shown. (*B*) Calculated surface density-titration experiment from conditions given in (*A*), using experimentally determined diffusion coefficients for monomers and dimers, showing that even weak dimerization up to $K_d = 25{,}000$ μm^{-2} should produce a detectable change in diffusion.

monomer and dimer diffusion coefficients (4.5 and 2.3 μm^2/s) and presumed brightness ratio between dimer and monomer of 2 were used. In this system, FCS provides an excellent dynamic range to detect from strong to exceptionally weak dimerization.

A series of density-dependent diffusion measurements of Ras by FCS (eGFP-labeled) on supported lipid bilayers are plotted alongside the LeuZ dimer calibration in Fig. 3 *A*. In these measurements, the supported membrane consisted of 20% PS, 80% DOPC, and a trace amount of Texas Red lipid probe, used as a benchmark standard to characterize the membrane integrity. PS is the major anionic lipid species found in the plasma membrane with the reported densities ranging between 10 and 20%. PS interacts directly with the hypervariable region of K-Ras4B and participates in stabilizing membrane association via electrostatic interactions (26).

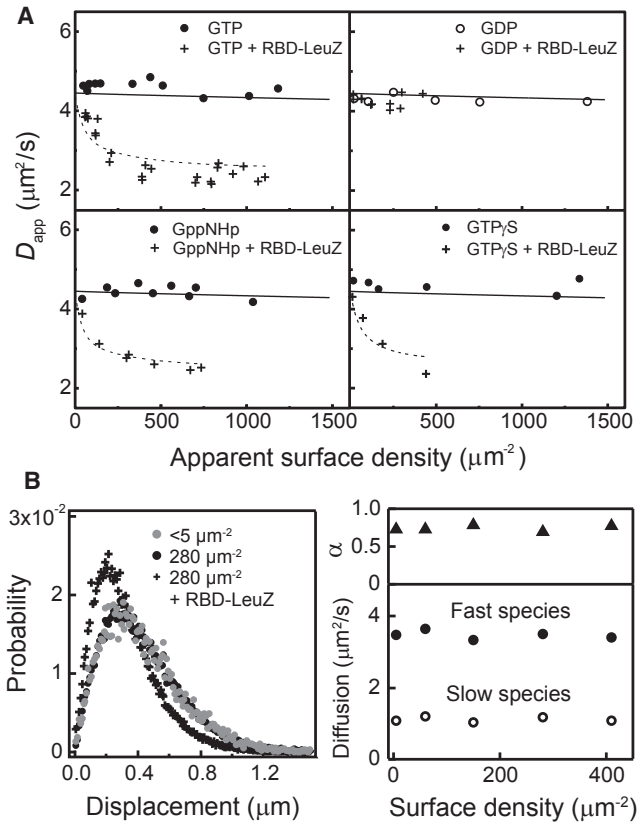

FIGURE 3 Density titration diffusion measurement on PS bilayers. (*A*) FCS measurements of eGFP-K-Ras4B in excess of various guanosine nucleotides were titrated on SLBs containing 20% PS bilayers, with and without 0.5 μM RBD-LeuZ cross linker. (*Solid lines*) Shown here is the diffusion change if the dimerization occurs with $K_d = 125{,}000\ \mu m^{-2}$, which is essentially a dense-packed concentration. (*Dotted lines*) Shown here are fits for cross-linked Ras, with K_d values ranging between 300 and 400 μm^{-2}. (*B*) (*Left*) Given here is the SMT step-size distribution for low- and high-density Ras, as well as high-density Ras with RBD-LeuZ. (*Right*) Given here are density-dependent diffusion coefficients D and fraction in faster species α for Ras without RBD-LeuZ. Both α and D of the two diffusing species are density-invariant, indicating that Ras dimerization does not occur under these circumstances.

GDP, GTP, and nonhydrolyzable GTP analogs GppNHp and GTPγS were tested to see if dimerization is dependent on the activation state Ras, as has been previously reported (22). To ensure that Ras was in the desired nucleotide state, the catalytic domain of guanosine exchange factor Son of Sevenless (SOS_{cat}) was included with excess nucleotide in solution. The FCS measurements indicate that for Ras alone, its diffusion remained independent of the surface density of 1500 μm^{-2} at ~4.5 μm^2/s. The solid lines through these data represent calculated FCS for $K_d = 1.25 \times 10^5\ \mu m^{-2}$, corresponding to no effective dimerization affinity. In contrast, GTP-, GppNHp-, and GTPγS-bound Ras shows a substantial decrease in diffusion in the presence of 0.5 μM RBD-LeuZ cross linker; the dotted lines represent calculated FCS data for fitted apparent K_d values, which ranged 300–400 μm^{-2}. GDP-bound Ras is density-independent even with RBD-LeuZ, as it is incapable of interacting with RBD.

The single-particle tracking results likewise illustrate that Ras by itself is monomeric on membrane surfaces. The step size distribution for Ras with and without RBD-LeuZ is plotted in Fig. 3 *B* (*left*). Ras shows essentially identical diffusion at low ($<1\ \mu m^{-2}$) and high (~280 μm^{-2}) surface densities. However, detailed analysis of the step size distribution, upon fitting to 2D Brownian diffusion, reveals the existence of two species of Ras on the membrane with differing mobilities: a major fast species with a diffusion coefficient of ~3.5 μm^2/s and minor slow species with ~1 μm^2/s (Fig. 3 *B*, *right*; also Fig. S8). Also, existence of the slow diffusing species is not due to dimerization. Even at extremely low total Ras surface density ($<1\ \mu m^{-2}$), where even high affinity dimers would not form, we observe both species in the mobility. In this extreme case, individual Ras molecules are several microns apart from each other, so they cannot interact to form dimers. Furthermore, the relative population for each diffusing state is density-invariant (as shown in Fig. 3 *B*, *right*). Based on these observations, we conclude that the two observed species likely reflect two different modes of protein-lipid interactions on the membrane surface, possibly with different numbers of anionic lipids making direct electrostatic contacts with the hypervariable region (9,45–47). If these additional interactions reorient the protein and enhance the degree of immersion of the protein to the membrane, they may substantially slow down the diffusion, as observed. In the presence of RBD-LeuZ, Ras forms dimers and the mobility is significantly reduced, as is evident in the step size distribution (Fig. 3 *B*, *left*). The differences in the measured diffusion constants between the SMT and FCS are systematic and determined by accuracy of instrumental calibration, but both are within the range of values reported for comparable systems (11,36,48).

The diffusion behavior of Ras was also observed to be strictly monomeric in the presence of various types of lipids.

The plasma membrane is a complex mixture of hundreds of phospholipid species as well as other components, and there have been reports suggesting that phospholipids with particular headgroups or chain chemistry may induce specific lateral organization of Ras. For example, it has been suggested that electrostatic lipid-protein interactions modulate orientation preference of K-Ras through charged membrane interaction surfaces in the G-domain, shifting the equilibrium toward specific dimer contacts (9,14,45); and asymmetric hydrocarbon chains corral Ras into clusters (49). We used DOPS (18:1-18:1), SOPS (18:0-18:1), DOPG, and PIP_2, whose chemical structures are shown in Fig. 4 *A*, to see if any of these produced Ras dimers. For the SLBs containing these lipids, the compositions were adjusted such that the overall nominal charge is −10%. The lack of detectable change in diffusion as a function of Ras density by FCS measurements (Fig. 4 *B*) demonstrates that Ras is monomeric within the accessible density range on these membranes, regardless of the various headgroups, chain chemistry, or the nucleotide state. For PIP_2, it has been reported that divalent cations such as Ca^{2+} can induce clustering of the lipids (50,51). However, in our system, the presence of 1 mM Ca^{2+} had no effect on the diffusion of Ras. The SMT step size distributions were also density-invariant for DOPG and PIP_2 bilayers when Ras is bound to GDP and GppNHp (Fig. 4 *C*).

Finally, cholesterol was introduced to the lipid membranes, as it has been reported that cholesterol may facilitate segregation Ras in the plasma membrane (8,49). Because it is difficult to make supported bilayers with cholesterol using the SUV rupture-fuse method, we instead used ruptured GUVs to create a planar patch of fluid bilayers (35,52–54). Fig. 5 *A* shows a typical batch of intact GUVs composed of unsaturated lipids (DOPC), saturated lipids (DPPC), charged lipids (DOPS or SOPS), and cholesterol, and a trace amount of TR-DHPE for imaging. As the nominal demixing temperature for this composition is 19°C, they showed single macroscopic phase at room temperature (30). Fig. 5, *B* and *C*, displays ruptured GUVs displaying the FCS focus and SMT trajectories in the identical experimental setup as the SLB cases. Diffusion measurements once again indicate that even with cholesterol, there is no density-dependent diffusion change in either FCS (Fig. 5 *D*) or SMT (Fig. 5 *E*). Thus Ras remains monomeric at all densities in the cholesterol-containing membrane.

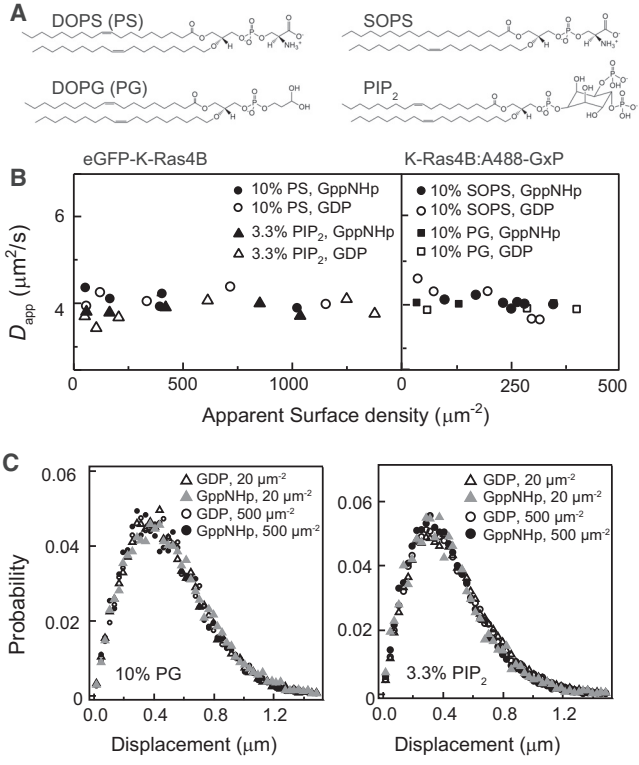

FIGURE 4 Effect of various lipids. (*A*) Chemical structures of anionic lipids used are shown. DOPS, SOPS, and DOPG have −1 nominal charge, and PIP_2 has −3 nominal charge. SOPS has asymmetric chains (18:0-18:1), whereas the others have symmetric chains (18:1-18:1). (*B*) FCS measurements of eGFP-K-Ras (*left*) and wild-type K-Ras (*right*) on SLBs containing these lipids (charge normalized to −10%) display density-independent diffusion, indicating a monomeric behavior. (*C*) SMT step size distributions are identical for high- and low-density K-Ras for DOPG or PIP_2 bilayers, regardless of the nucleotide states.

CONCLUSION

In summary, we have shown that in supported lipid bilayers, K-Ras4B by itself remains monomeric over a wide range of surface densities in multiple types of membrane compositions. Careful diffusion measurements by FCS and SMT show that Ras has a density-independent diffusion with the value comparable to the lipids up to surface densities

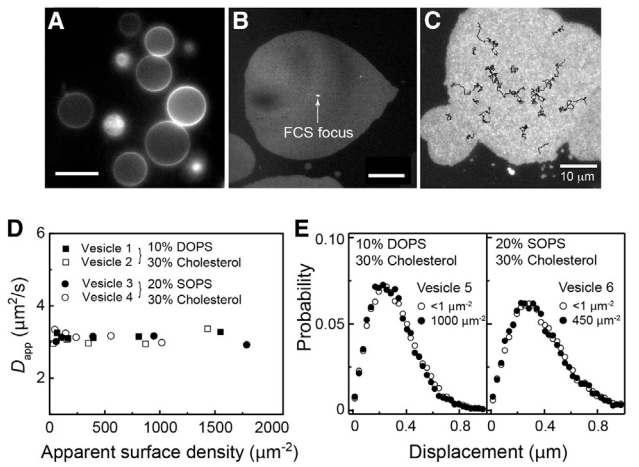

FIGURE 5 Effect of cholesterol. (*A*) Intact GUVs were ruptured onto a glass surface to create patches of bilayers containing cholesterol for FCS (*B*, focus spot shown) and SMT (*C*, particle trajectories shown) diffusion measurements. Scale bar: 10 μm. (*D*) Shown here are FCS measurements for (*B*). (*E*) Shown here are SMT measurements for (*C*). K-Ras diffusion is density-independent for all cases.

of nearly dense-packed. This means that the clusters and assemblies of Ras observed in live cell contexts are probably driven by interactions with other proteins, such as scaffolding proteins or downstream effectors. Another factor that may influence the lateral organization of Ras, but has not been experimentally examined here, is the topological membrane fluctuations. The supported lipid bilayers are held in a planar configuration by the glass support, and large membrane undulations are damped (55). However, it is not clear whether such large undulations would occur in cells, where they are expected to be damped by the cortical cytoskeleton.

SUPPORTING MATERIAL

Supporting Materials and Methods and nine figures are available at http://www.biophysj.org/biophysj/supplemental/S0006-3495(17)31205-5.

AUTHOR CONTRIBUTIONS

J.K.C., Y.K.L., and J.T.G. designed research and wrote the paper; J.K.C. and Y.K.L performed research and analyzed data; J.-P.D., W.K.G., S.A., and A.G.S. contributed new reagents.

ACKNOWLEDGMENTS

We thank Jennifer Mehalko, Cammi Bittner, Zhaojing Meng, and Cheryl Habrukowich for technical support in the preparation and characterization of the K-Ras proteins, and Dr. Scott D. Hansen, Dr. Luke M. Oltrogge, and Dr. William Y.C. Huang for critical reading of the manuscript.

Primary support for this project was provided by the National Cancer Institute (NCI), National Institutes of Health (NIH), under contract U01CA202241 to J.T.G. Additional support to A.G.S. was provided by the National Cancer Institute (NCI)), National Institutes of Health (NIH) under contract HHSN261200800001E. The content of this publication does not necessarily reflect the views or policies of the Department of Health and Human Services, nor does mention of trade names, commercial products, or organizations imply endorsement by the U.S. Government.

REFERENCES

1. Bollag, G., and F. McCormick. 1991. Regulators and effectors of Ras proteins. *Annu. Rev. Cell Biol.* 7:601–632.
2. Plowman, S. J., C. Muncke, …, J. F. Hancock. 2005. H-Ras, K-Ras, and inner plasma membrane raft proteins operate in nanoclusters with differential dependence on the actin cytoskeleton. *Proc. Natl. Acad. Sci. USA.* 102:15500–15505.
3. Prior, I. A., and J. F. Hancock. 2012. Ras trafficking, localization and compartmentalized signalling. *Semin. Cell Dev. Biol.* 23:145–153.
4. Santos, E. 2014. Dimerization opens new avenues into Ras signaling research. *Sci. Signal.* 7:pe12.
5. Chen, M., A. Peters, …, X. Nan. 2016. Ras dimer formation as a new signaling mechanism and potential cancer therapeutic target. *Mini Rev. Med. Chem.* 16:391–403.
6. Stephen, A. G., D. Esposito, …, F. McCormick. 2014. Dragging Ras back in the ring. *Cancer Cell.* 25:272–281.
7. Spencer-Smith, R., A. Koide, …, J. P. O'Bryan. 2017. Inhibition of RAS function through targeting an allosteric regulatory site. *Nat. Chem. Biol.* 13:62–68.
8. Janosi, L., Z. Li, …, A. A. Gorfe. 2012. Organization, dynamics, and segregation of Ras nanoclusters in membrane domains. *Proc. Natl. Acad. Sci. USA.* 109:8097–8102.
9. Sayyed-Ahmad, A., K. J. Cho, …, A. A. Gorfe. 2016. Computational equilibrium thermodynamic and kinetic analysis of K-Ras dimerization through an effector binding surface suggests limited functional role. *J. Phys. Chem. B.* 120:8547–8556.
10. Güldenhaupt, J., T. Rudack, …, K. Gerwert. 2012. N-Ras forms dimers at POPC membranes. *Biophys. J.* 103:1585–1593.
11. Lin, W. C., L. Iversen, …, J. T. Groves. 2014. H-Ras forms dimers on membrane surfaces via a protein-protein interface. *Proc. Natl. Acad. Sci. USA.* 111:2996–3001.
12. Abankwa, D., A. A. Gorfe, …, J. F. Hancock. 2010. Ras membrane orientation and nanodomain localization generate isoform diversity. *Proc. Natl. Acad. Sci. USA.* 107:1130–1135.
13. Cho, K. J., and J. F. Hancock. 2013. Ras nanoclusters: a new drug target? *Small GTPases.* 4:57–60.
14. Prakash, P., Y. Zhou, …, A. A. Gorfe. 2016. Oncogenic K-Ras binds to an anionic membrane in two distinct orientations: a molecular dynamics analysis. *Biophys. J.* 110:1125–1138.
15. Zhou, Y., C. O. Wong, …, J. F. Hancock. 2015. SIGNAL TRANSDUCTION. Membrane potential modulates plasma membrane phospholipid dynamics and K-Ras signaling. *Science.* 349:873–876.
16. Hancock, J. F. 2003. Ras proteins: different signals from different locations. *Nat. Rev. Mol. Cell Biol.* 4:373–384.
17. Nan, X., T. M. Tamgüney, …, S. Chu. 2015. Ras-GTP dimers activate the mitogen-activated protein kinase (MAPK) pathway. *Proc. Natl. Acad. Sci. USA.* 112:7996–8001.
18. Šolman, M., A. Ligabue, …, D. Abankwa. 2015. Specific cancer-associated mutations in the switch III region of Ras increase tumorigenicity by nanocluster augmentation. *ELife.* 4:e08905.
19. Blazevits, O., Y. G. Mideksa, …, D. Abankwa. 2016. Galectin-1 dimers can scaffold Raf-effectors to increase H-Ras nanoclustering. *Sci. Rep.* 6:24165.
20. Guzmán, C., M. Šolman, …, D. Abankwa. 2014. The efficacy of Raf kinase recruitment to the GTPase H-Ras depends on H-Ras membrane conformer-specific nanoclustering. *J. Biol. Chem.* 289:9519–9533.
21. Chung, J. K., Y. K. Lee, …, J. T. Groves. 2016. Covalent Ras dimerization on membrane surfaces through photosensitized oxidation. *J. Am. Chem. Soc.* 138:1800–1803.
22. Muratcioglu, S., T. S. Chavan, …, R. Nussinov. 2015. GTP-dependent K-Ras dimerization. *Structure.* 23:1325–1335.
23. Kovrigina, E. A., A. R. Galiakhmetov, and E. L. Kovrigin. 2015. The Ras G domain lacks the intrinsic propensity to form dimers. *Biophys. J.* 109:1000–1008.
24. Pylayeva-Gupta, Y., E. Grabocka, and D. Bar-Sagi. 2011. RAS oncogenes: weaving a tumorigenic web. *Nat. Rev. Cancer.* 11:761–774.
25. Gillette, W. K., D. Esposito, …, A. G. Stephen. 2015. Farnesylated and methylated KRAS4b: high yield production of protein suitable for biophysical studies of prenylated protein-lipid interactions. *Sci. Rep.* 5:15916.
26. Ahearn, I. M., K. Haigis, …, M. R. Philips. 2011. Regulating the regulator: post-translational modification of Ras. *Nat. Rev. Mol. Cell Biol.* 13:39–51.
27. Sondermann, H., S. M. Soisson, …, J. Kuriyan. 2004. Structural analysis of autoinhibition in the Ras activator Son of Sevenless. *Cell.* 119:393–405.
28. Lin, W. C., C. H. Yu, …, J. T. Groves. 2010. Supported membrane formation, characterization, functionalization, and patterning for application in biological science and technology. *Curr. Protoc. Chem. Biol.* 2:235–269.
29. Schmid, E. M., D. L. Richmond, and D. A. Fletcher. 2015. Reconstitution of proteins on electroformed giant unilamellar vesicles. *Methods Cell Biol.* 128:319–338.

30. Veatch, S. L., and S. L. Keller. 2003. Separation of liquid phases in giant vesicles of ternary mixtures of phospholipids and cholesterol. *Biophys. J.* 85:3074–3083.

31. Iversen, L., H. L. Tu, …, J. T. Groves. 2014. Molecular kinetics. Ras activation by SOS: allosteric regulation by altered fluctuation dynamics. *Science.* 345:50–54.

32. Lee, Y. K., S. T. Low-Nam, …, J. T. Groves. 2017. Mechanism of SOS PR-domain autoinhibition revealed by single-molecule assays on native protein from lysate. *Nat. Commun.* 8:15061.

33. Lakowicz, J. R. 2006. Principles of Fluorescence Spectroscopy. Springer, New York, NY.

34. Saffman, P. G., and M. Delbrück. 1975. Brownian motion in biological membranes. *Proc. Natl. Acad. Sci. USA.* 72:3111–3113.

35. Kaizuka, Y., and J. T. Groves. 2004. Structure and dynamics of supported intermembrane junctions. *Biophys. J.* 86:905–912.

36. Knight, J. D., M. G. Lerner, …, J. J. Falke. 2010. Single molecule diffusion of membrane-bound proteins: window into lipid contacts and bilayer dynamics. *Biophys. J.* 99:2879–2887.

37. Ziemba, B. P., and J. J. Falke. 2013. Lateral diffusion of peripheral membrane proteins on supported lipid bilayers is controlled by the additive frictional drags of (1) bound lipids and (2) protein domains penetrating into the bilayer hydrocarbon core. *Chem. Phys. Lipids.* 172-173:67–77.

38. Ziemba, B. P., J. D. Knight, and J. J. Falke. 2012. Assembly of membrane-bound protein complexes: detection and analysis by single molecule diffusion. *Biochemistry.* 51:1638–1647.

39. Wu, Y., J. Vendome, …, B. Honig. 2011. Transforming binding affinities from three dimensions to two with application to cadherin clustering. *Nature.* 475:510–513.

40. Kapoor, S., G. Triola, …, R. Winter. 2012. Revealing conformational substates of lipidated N-Ras protein by pressure modulation. *Proc. Natl. Acad. Sci. USA.* 109:460–465.

41. Gorfe, A. A., A. Babakhani, and J. A. McCammon. 2007. Free energy profile of H-Ras membrane anchor upon membrane insertion. *Angew. Chem. Int. Ed. Engl.* 46:8234–8237.

42. Gorfe, A. A., A. Babakhani, and J. A. McCammon. 2007. H-Ras protein in a bilayer: interaction and structure perturbation. *J. Am. Chem. Soc.* 129:12280–12286.

43. Gorfe, A. A., M. Hanzal-Bayer, …, J. A. McCammon. 2007. Structure and dynamics of the full-length lipid-modified H-Ras protein in a 1,2-dimyristoylglycero-3-phosphocholine bilayer. *J. Med. Chem.* 50:674–684.

44. Pai, E. F., W. Kabsch, …, A. Wittinghofer. 1989. Structure of the guanine-nucleotide-binding domain of the Ha-Ras oncogene product p21 in the triphosphate conformation. *Nature.* 341:209–214.

45. Mazhab-Jafari, M. T., C. B. Marshall, …, M. Ikura. 2015. Oncogenic and RASopathy-associated K-RAS mutations relieve membrane-dependent occlusion of the effector-binding site. *Proc. Natl. Acad. Sci. USA.* 112:6625–6630.

46. Li, Z. L., and M. Buck. 2017. Computational modeling reveals that signaling lipids modulate the orientation of K-Ras4A at the membrane reflecting protein topology. *Structure.* 25:679–689.e2.

47. Janosi, L., and A. A. Gorfe. 2010. Segregation of negatively charged phospholipids by the polycationic and farnesylated membrane anchor of K-Ras. *Biophys. J.* 99:3666–3674.

48. Ries, J., S. Chiantia, and P. Schwille. 2009. Accurate determination of membrane dynamics with line-scan FCS. *Biophys. J.* 96:1999–2008.

49. Zhou, Y., P. Prakash, …, J. F. Hancock. 2017. Lipid-sorting specificity encoded in K-Ras membrane anchor regulates signal output. *Cell.* 168:239–251.e16.

50. Bilkova, E., R. Pleskot, …, Ü. Coskun. 2017. Calcium directly regulates phosphatidylinositol 4,5-bisphosphate headgroup conformation and recognition. *J. Am. Chem. Soc.* 139:4019–4024.

51. Levental, I., D. A. Christian, …, P. A. Janmey. 2009. Calcium-dependent lateral organization in phosphatidylinositol 4,5-bisphosphate (PIP_2)- and cholesterol-containing monolayers. *Biochemistry.* 48:8241–8248.

52. Wong, A. P., and J. T. Groves. 2001. Topographical imaging of an intermembrane junction by combined fluorescence interference and energy transfer microscopies. *J. Am. Chem. Soc.* 123:12414–12415.

53. Parthasarathy, R., and J. T. Groves. 2004. Protein patterns at lipid bilayer junctions. *Proc. Natl. Acad. Sci. USA.* 101:12798–12803.

54. Parthasarathy, R., C. H. Yu, and J. T. Groves. 2006. Curvature-modulated phase separation in lipid bilayer membranes. *Langmuir.* 22:5095–5099.

55. Kaizuka, Y., and J. T. Groves. 2006. Hydrodynamic damping of membrane thermal fluctuations near surfaces imaged by fluorescence interference microscopy. *Phys. Rev. Lett.* 96:118101.

Biophysical Journal, Volume *114*

Supplemental Information

K-Ras4B Remains Monomeric on Membranes over a Wide Range of Surface Densities and Lipid Compositions

Jean K. Chung, Young Kwang Lee, John-Paul Denson, William K. Gillette, Steven Alvarez, Andrew G. Stephen, and Jay T. Groves

Supporting Information for:

Membrane-reconstituted K-Ras4B remains monomeric over a wide range of surface densities and membrane lipid compositions

Contents

A. Characterization of the full-length K-Ras

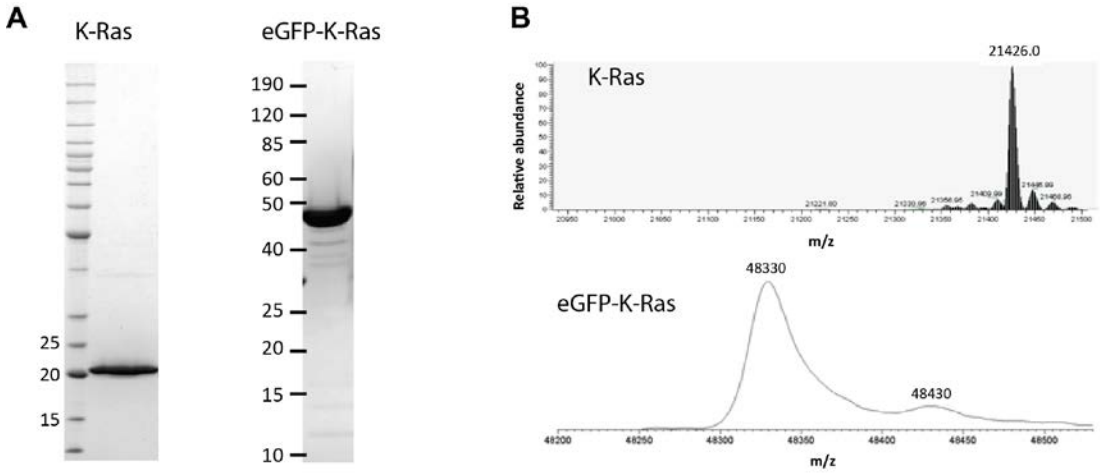

Figure S1 Characterization of processed K-Ras and eGFP-K-Ras. (A) SDS-PAGE analysis, **(B)** intact electrospray ionization mass spectrometry of the fully processed K-Ras4B constructs. The theoretical molecular weight of K-Ras4B and eGFP-KRas4B are 21426 and 48330 Da, respectively. The minor species observed at 48430 for eGFP-KRas4B is a 100 Da adduct formed during the liquid chromatography (LC) step prior to ESI-MS analysis. This species is not present when the sample is directly injected for ESI-MS analysis, bypassing the LC system.

The amino acid sequence for K-Ras4B after processing, including the farnesylation and methylation is:

GGSGTEYKLVVVGAGGVGKSALTIQLIQNHFVDEYDPTIEDSYRKQVVIDGETCLLDILDTAGQEEYSAMRDQYMRTGE
GFLCVFAINNTKSFEDIHHYREQIKRVKDSEDVPMVLVGNKCDLPSRTVDTKQAQDLARSYGIPFIETSAKTRQGVDDAF
YTLVREIRKHKEKMSKDGKKKKKKSKTKC-FMe

The residues remaining after TEV cleavage are shown in red. The underlined Thr is the first amino acid in the K-Ras4B sequence. The final molecular weight is 21426 Da.

For eGFP-labeled K-Ras, the final amino acid sequence is:

GMVSKGEELFTGVVPILVELDGDVNGHKFSVSGEGEGDATYGKLTLKFICTTGKLPVPWPTLVTTLTYGVQCFSRYPDH
MKQHDFFKSAMPEGYVQERTIFFKDDGNYKTRAEVKFEGDTLVNRIELKGIDFKEDGNILGHKLEYNYNSHNVYIMADK
QKNGIKVNFKIRHNIEDGSVQLADHYQQNTPIGDGPVLLPDNHYLSTQSALSKDPNEKRDHMVLLEFVTAAGITLGMD
ELYKGSGTEYKLVVVGAGGVGKSALTIQLIQNHFVDEYDPTIEDSYRKQVVIDGETCLLDILDTAGQEEYSAMRDQYMRT
GEGFLCVFAINNTKSFEDIHHYREQIKRVKDSEDVPMVLVGNKCDLPSRTVDTKQAQDLARSYGIPFIETSAKTRQGVDD
AFYTLVREIRKHKEKMSKDGKKKKKKSKTKC-FMe

The linker sequence is shown in red. The final molecular weight for this construct after farnesylation and methylation is 48330 Da.

B. K-Ras equilibration to supported lipid bilayers

Upon introduction to supported lipid bilayer, K-Ras spontaneously inserts itself to the membrane and reaches stable equilibrium in ~10 minutes. The membrane binding kinetics showed no difference between GDP- and GTP-bound states.

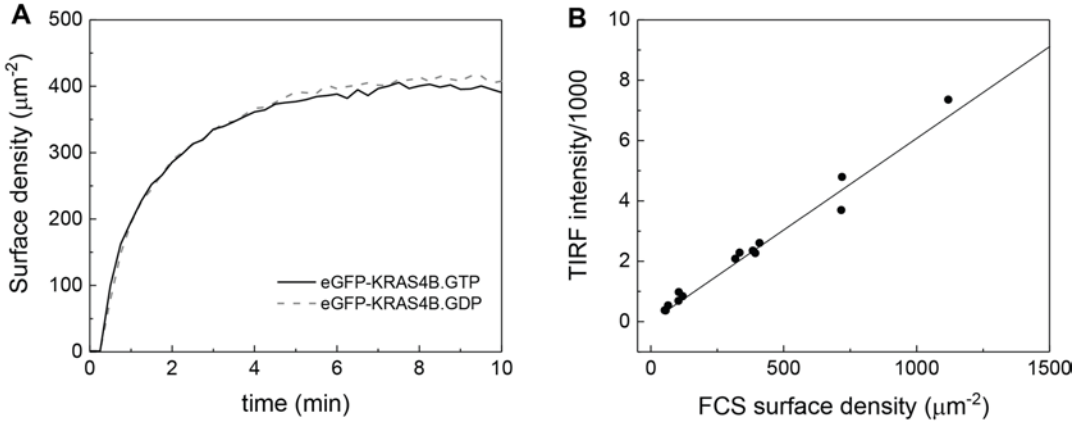

Figure S2 Spontaneous insertion of eGFP-labeled K-Ras4B onto supported lipid bilayer. A The adsorption of 40 nM GTP- and GDP-bound K-Ras onto 10% PS bilayer, monitored by TIRF microscopy. **B** The TIRF intensity was calibrated to the surface density of eGFP-KRas4B by correlating FCS surface density measurements to the TIRF intensity. Within the experimental range, the TIRF intensity increased linearly with the number of K-Ras on the membrane surface.

C. Experimental precision for FCS

Here, we will discuss the experimental precision for the FCS measurements on supported lipid bilayers. For each sample condition, four spots in the SLB's are measured, at least 1 μm apart from each other. Each autocorrelation trace is average of 10 scans of 5 seconds. Shown below are autocorrelation data obtained from low-density eGFP-KRas4B.GTP:

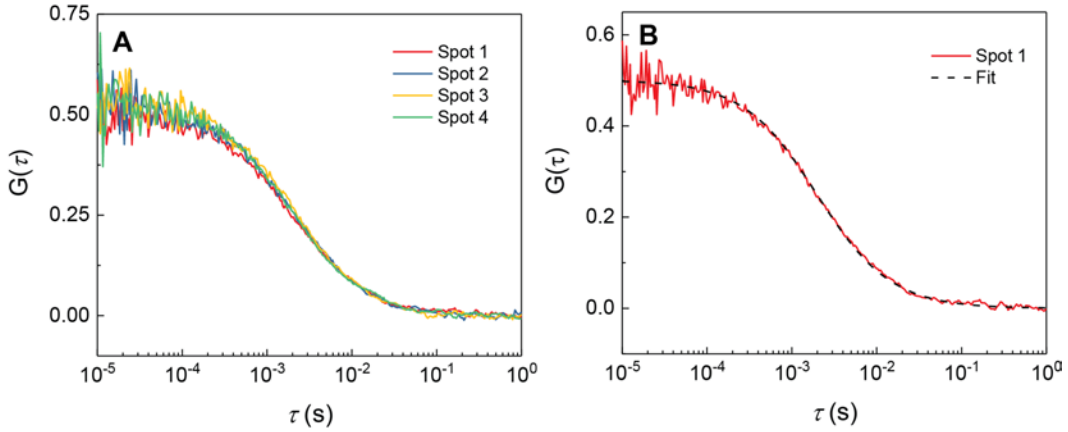

Figure S3 FCS experimental precision. **A** Ten 5-scan averages were collected for four spots in the supported lipid bilayer sample. **B** Autocorrelation data from Spot 1 was fit to Equation 1.

Autocorrelation functions collected from four spots in the sample are displayed in Figure S2A. Then, each autocorrelation function is fit to 2D Gaussian diffusion model, Equation 1, shown in Figure S2B, and the residence time τ_d and N are obtained. The table below summarizes fit values from each autocorrelation function.

Spot	τ_d (ms)	N
1	1.97	2.00
2	1.91	1.91
3	1.93	1.86
4	1.85	1.88
Average	1.91	1.91
Standard error	0.025	0.030

For this set of measurements, the standard error for the fit values were less than 2% for both τ_d and N. Each data point shown in FCS measurements such as Figure 2A represent the average of 3-4 spots such as these. The standard error was no more than 5% for all of data presented in this work. The scatter in the data may reflect actual heterogeneities in the bilayer samples, which could have had uneven areas in the glass substrates, on top of some day-to-day variations.

D. Estimating diffusion coefficients for monomeric and dimeric Ras

To determine the diffusion coefficients for Ras monomers and dimers, we titrated Ras surface density in excess RBD-LeuZ crosslinker, and examined the changing diffusion rates. At very low Ras density, the diffusion coefficient was approximately 4.5 μm^{-2}, which is same as Ras without the crosslinker—therefore, this is the diffusion coefficient of Ras monomer. Then, as Ras surface density increases, diffusion decreases crosslinked species begin to appear.

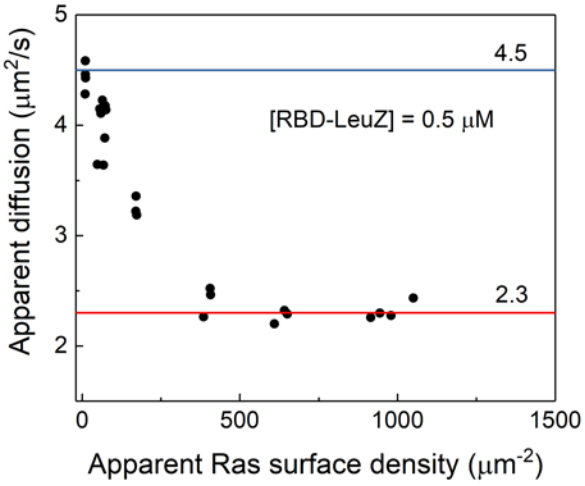

Figure S4 FCS diffusion measurement for monomeric and dimeric Ras using RBD-LeuZ crosslinker.

As the apparent density approaches the detection limit (~1500 μm^{-2}), the diffusion coefficient value is observed to plateau near 2.3 $\mu m^2/s$. In principle, it is unknown whether all Ras are dimeric at this point, as the dimer fraction for this crosslinking reaction is convolution of the binding affinities between Ras:RBD and LeuZ:LeuZ. Presumably, there is a regime of Ras surface density and RBD-LeuZ concentration where all Ras are crosslinked, but it is unknown whether these experimental conditions are within that zone. Still, 2.3 $\mu m^2/s$ provides a reasonable approximation, and it is close to the decreased diffusion value by dimerization observed in other systems (41). Furthermore, since this is an upper limit for the true diffusion coefficient of the dimer, all calculations performed with this value generally resulted in conservative estimates in differentiating dimers from monomers.

E. Calculating FCS binding curve for two-dimensional dimerization reaction

In this section, theoretical FCS diffusion measurements for two-dimensional dimerization reactions with arbitrary dissociation constants will be discussed. These are details pertaining to Figure 2 in the main text. Because both molecular brightness and diffusion change due to dimerization, its effect on the shape of the binding curve is not straightforward.

As discussed in the text, Ras dimerization on a membrane surface can be considered as a simple bimolecular reaction,

$$2Ras \leftrightarrow Ras \cdot Ras \qquad \text{(S1)}$$

Then, the two-dimensional dissociation constant K_d is defined as

$$K_d = [Ras]^2 / [Ras \cdot Ras] \qquad \text{(S2)}$$

Where [*Ras*] and [*Ras*·*Ras*] denote the two-dimensional surface density for monomers and dimers, respectively. For simplicity's sake, let us denote the surface density of monomers, dimers, and total Ras molecules as X_m, X_d, and X, respectively, such that $X = X_m + 2X_d$. The surface density of dimers X_d as a function of surface density X is given by

$$X_d = \frac{1}{8}\left(K_d + 4X - \sqrt{K_d(K_d + 8X)}\right) \qquad \text{(S3)}$$

The derivation for this expression can be found in (11). For a hypothetical dimerization reaction with K_d = 200 μm^{-2}, the theoretical "binding curve" can be visualized as follows:

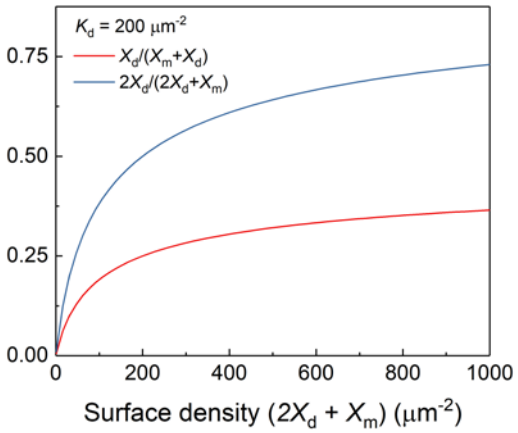

Figure S5 Calculated dimer fractions from Equation S3 for K_d = 200 μm^{-2}.

Here, we make the distinction between two types of dimer fractions: *numerical* dimer fraction, $X_d/(X_d + X_m)$, and *chemical* dimer fraction, $2X_d/(2X_d + X_m)$. While the chemical dimer fraction is the quantity of interest for the dimerization reaction, numerical dimer fraction is more directly relevant to the FCS observables, as the N value obtained from FCS is sensitive (for the most part) only to the number of diffusing particles regardless of their identity.

For a sample with two different molecular brightness B_1 and B_2, and two-dimensional Gaussian focus residence time of τ_1 and τ_2, the autocorrelation function $G(\tau)$ is given by:

$$G(\tau) = \frac{N_1 B_1^2 (1+\tau/\tau_1)^{-1} + N_2 B_2^2 (1+\tau/\tau_2)^{-1}}{(N_1 B_1 + N_2 B_2)^2} \qquad \text{(S4)}$$

Where N, B, τ, are number of particles, molecular brightness, and focus residence time, respectively (33). This equation is a form of Equation 5 for two components. One consequence of this relation is that the autocorrelation is strongly weighted by the brighter species in the sample. Let us consider a hypothetical mixture of monomers and dimers, with $B_1 = 1$, $B_2 = 2$, $D_1 = 4.5$ μm^2/s, and $D_2 = 2.3$ μm^2/s, where the subscripts 1 and 2 correspond to monomers and dimers, for a spot size of $w = 200$ nm. Then, $G(\tau)$ for purely monomeric (red), purely dimeric (blue), and equal population of monomers and dimers (broken green line) can be calculated using Equation S4:

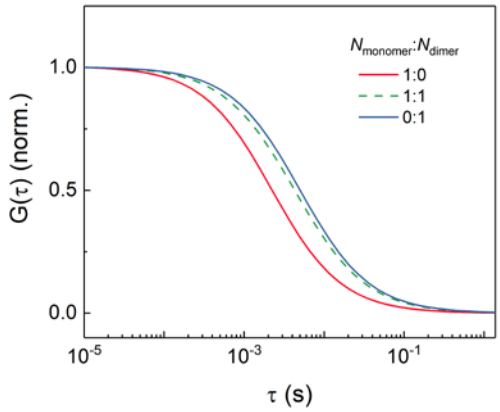

Figure S6 Calculated FCS autocorrelation for mixed populations.

Due to the brightness effect, the autocorrelation for 1:1 mixture is clearly not the average of the monomers and dimers, but is much closer to the autocorrelation function for the purely dimeric population, because the slower and twice-brighter dimers are much more strongly represented. Fitting this autocorrelation to a single-species model, Equation 1, yields:

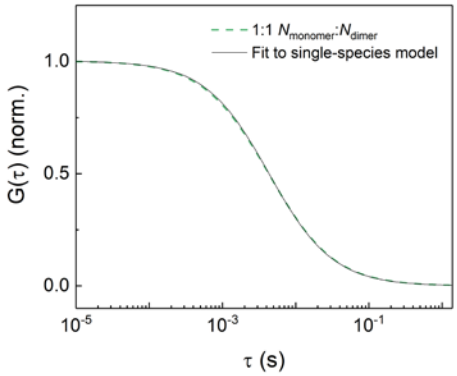

Figure S7 Single-species fitting to mixed population autocorrelation function.

Even with the calculated, noiseless two-population $G(\tau)$, the single species model fit is nearly perfect: this due to the gently sloping lineshape of the FCS autocorrelation function. The apparent diffusion coefficient from this fit is 2.6 $\mu m^2/s$.

By performing same simulations for each particle density, we can calculate a theoretical FCS experiment. Note that this is not an analytical calculation, because there is no analytical solution for 1-species model (Equation 1) for two-species autocorrelation function (Equation S4). Therefore, this calculation is a numerical estimation based on optimization.

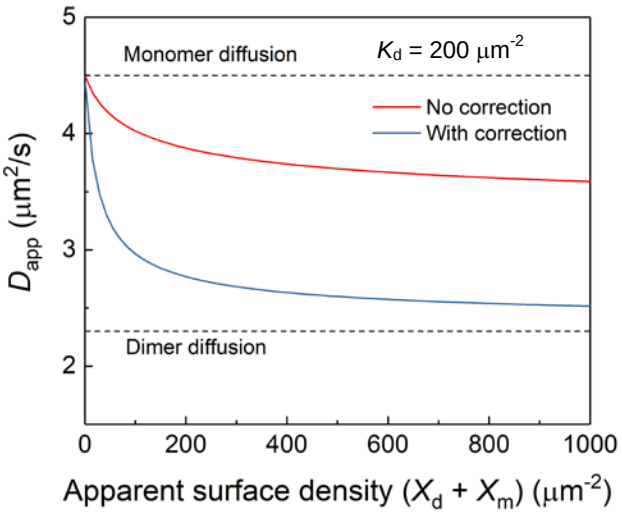

Figure S8 Simulated FCS binding curve with the brightness effect correction.

Here, the apparent diffusion coefficient for two-species autocorrelation function are shown in (blue). This is contrasted to the case in which there is no nonlinear contribution from unequal molecular brightness (*i.e.* if $B_1 = B_2$). This comparison highlights the fact that dimers are much more readily detected in an FCS experiment than would be otherwise, giving it a wide effective dynamic range. Note that for the *x*-axis for this calculated experiment is *apparent* surface density $X_d + X_m$ as would have been obtained from the FCS autocorrelation function. For Figure 2B in the main text, same calculations were performed for a series of K_d values.

F. Estimating 3-dimensional concentration from 2-dimensional surface density

Here, we will outline how three-dimensional concentration from two-dimensional surface density may be estimated. More details can be found in (11). The translational entropy, or the entropy of mixing, is determined only by the fractional occupation. In other words,

% occupied volume in 3D = % occupied area in 2D

For Ras in solution, the unit volume encasing the protein is approximately 3 nm-cube, and the equivalent area on membranes is a 3 nm-square. Then, for surface density of x μm^{-2}, the fraction of occupied area is

$$(3\,\mathrm{nm})^2 \times x\,\mu\mathrm{m}^{-2} \times (1\,\mu\mathrm{m}^2/10^6\,\mathrm{nm}^2) = (9\times10^{-6})x$$

For one liter, the volume occupied by Ras is

$$1\,\mathrm{L} \times (9 \times 10^{-6})x \times (10^{24}\,\mathrm{nm}^3/1\mathrm{L}) = (9 \times 10^{18})x\ \mathrm{nm}^3$$

And the number of Ras in this volume is

$$(9\times10^{18})x\ \mathrm{nm}^3 \times \frac{1\ \mathrm{Ras}}{(3\ \mathrm{nm})^3} \times \frac{1\ \mathrm{mol}}{6.022\times10^{23}\ \mathrm{Ras}} = (6\times10^{-7})x\ \mathrm{mol}$$

Therefore, for Ras, two-dimensional surface density x μm^{-2} is equivalent to 0.6 x μM.

G. Single molecule trajectory analysis

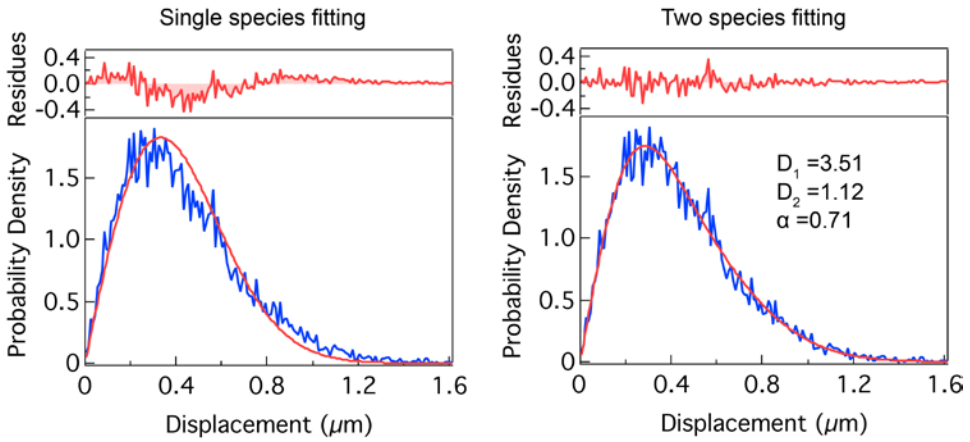

Figure S9. A single and two species fitting of step size distribution of K-Ras. A single species model (Equation 3 with $\alpha = 1$) yields systematic fitting residues and fails to describe the step size distribution. However, two species model (Equation 3) adequately describe the distribution. The distribution was acquired with 100 pM K-Ras labeled with GppNHp-AF647 on a 20% DOPS and 80% DOPC membrane at 20 ms frame rate.